BIOPHYSICS

ULK1 forms distinct oligomeric states and nanoscopic structures during autophagy initiation

Chiranjib Banerjee[1], Dushyant Mehra[1,2], Daihyun Song[3], Angel Mancebo[1], Ji-Man Park[3], Do-Hyung Kim[3]*, Elias M. Puchner[1]*

Autophagy induction involves extensive molecular and membrane reorganization. Despite substantial progress, the mechanism underlying autophagy initiation remains poorly understood. Here, we used quantitative photoactivated localization microscopy with single-molecule sensitivity to analyze the nanoscopic distribution of endogenous ULK1, the kinase that triggers autophagy. Under amino acid starvation, ULK1 formed large clusters containing up to 161 molecules at the endoplasmic reticulum. Cross-correlation analysis revealed that ULK1 clusters engaging in autophagosome formation require 30 or more molecules. The ULK1 structures with more than the threshold number contained varying levels of Atg13, Atg14, Atg16, LC3B, GEC1, and WIPI2. We found that ULK1 activity is dispensable for the initial clustering of ULK1, but necessary for the subsequent expansion of the clusters, which involves interaction with Atg14, Atg16, and LC3B and relies on Vps34 activity. This quantitative analysis at the single-molecule level has provided unprecedented insights into the behavior of ULK1 during autophagy initiation.

INTRODUCTION

Macroautophagy (hereafter referred to as autophagy) is an evolutionarily conserved process in eukaryotic cells that degrades intracellular organelles and macromolecules in the lysosome. Autophagy plays a fundamental role in maintaining the cellular homeostasis via controlling degradation and recycling of cellular constituents. Dysregulation of autophagy is related to a broad range of diseases, including cancer, neurodegeneration, and diabetes (1, 2). Autophagy is mainly induced under amino acid starvation or other stress conditions via suppression of mechanistic target of rapamycin complex 1 (mTORC1), the central nutrient-sensitive protein kinase complex, and subsequent activation of UNC51-like kinase 1 (ULK1), the protein kinase that triggers molecule events necessary for autophagy initiation (3–8). Despite the extensive studies on autophagy mechanisms, our understanding of the autophagy initiation process remains still limited largely due to the complex nature of the process.

Autophagy is an extensive membrane process that starts with the formation of the double-membrane structure called phagophore. The phagophore membrane grows and develops into the closed double-membrane structure called autophagosome that encompasses cargos destined to the lysosome (9–11). According to the prevalent model, autophagosome formation starts at the endoplasmic reticulum (ER) exit sites or the ER-mitochondria contact sites with the formation of the phagophore. The phagophore membrane has also been shown to originate from late endosomes or lysosomes, the Golgi complex, as well as mitochondria (9–11). The key step for autophagosome formation is activation of ULK1 (5–8). ULK1 forms a large protein complex by interacting with Atg13 (autophagy-related protein 13), FIP200 (FAK family kinase interacting protein

200 kDa), and Atg101 (5–8, 12–15). ULK1 mostly localizes on the ER or Atg9 compartments (16) and forms puncta in the cytoplasm of starved cells before the formation of the phagophore (17–19). This suggests that understanding how ULK1 puncta form in response to starvation is key to better understand the autophagy initiation process.

Prior studies using confocal or other conventional fluorescence microscopy techniques have provided useful but limited knowledge on the nature of ULK1 puncta because of their limited spatial resolution and lack of single-molecule sensitivity. Recently, highly sensitive single-molecule and superresolution microscopy techniques have been developed, enabling the study of autophagy below the optical diffraction limit (20). For instance, structured illumination microscopy (SIM) is a fast technique for imaging living cells, achieves a lateral resolution of ~100 nm, and has yielded substantial insights into autophagy and its initiation process (18, 21–23). Recently, Chen et al. (24) used SIM to quantify the interaction of lysosomes with mitochondria during mitophagy with increased resolution. Stimulated emission depletion (STED) microscopy (25) offers a higher resolution of ~50 nm, is also compatible with live cell imaging, but comes at the cost of scanning a high-power excitation and depletion laser beam across the sample. This technique was recently used to study alternative autophagy at the Golgi and enabled to detect translocation of WIPI3 puncta from the cytoplasm to the trans-Golgi (26). STED also yielded insights into the initiation of autophagosome formation by monitoring LC3B puncta at contact sites between the plasma membrane and the ER contact sites (27).

The highest resolution of ~20 nm can be achieved by single-molecule localization microscopy techniques. However, because of the long data acquisition time, they are mostly applied in fixed cells for high-resolution studies. Stochastic optical reconstruction microscopy (STORM) (16, 28), for instance, has advanced our understanding of the autophagy initiation process by enabling differentiation of structures with small sizes that cannot be resolved by other techniques. Using STORM, Karanasios et al. (16) resolved small Atg13 clusters and tracked their maturation during

[1]School of Physics and Astronomy, University of Minnesota, Twin Cities, Minneapolis, MN, USA. [2]Department of Biomedical Engineering and Physiology, Mayo Clinic, Rochester, MN, USA. [3]Department of Biochemistry, Molecular Biology, and Biophysics, University of Minnesota, Twin Cities, Minneapolis, MN, USA.
*Corresponding author. Email: epuchner@umn.edu (E.M.P.); dhkim@umn.edu (D.-H.K.)

autophagy, shedding light on the transient participation of Atg9 during autophagy initiation. Photoactivated localization microscopy (PALM) offers a comparable resolution to STED and STORM but can provide additional information about the stoichiometry of protein complexes and the quantification of biomolecules in intracellular structures (*29–35*). In particular, quantitative photoactivated localization microscopy (qPALM) (*36, 37*) using irreversibly bleaching photoconvertible or photoswitchable fluorescent proteins (PSFPs) can be combined with endogenous tagging, e.g., using CRISPR-Cas9, to quantify native molecule numbers in protein clusters or intracellular structures. Various analysis techniques have also been developed for PALM to determine the precise spatial distribution of signaling proteins (*38, 39*).

Most fluorescence and superresolution microscopy studies conducted with mammalian cells have relied on overexpression of fluorescently tagged proteins (*40*). Overexpression can cause artifacts in determining the oligomeric state and spatial distribution of proteins (*41*). Many proteins involved in autophagy function as protein complexes. Thus, overexpressing autophagy proteins can disturb the stoichiometry of the complexes as well as the integrity of the autophagy pathway. In addition, overexpression itself can alter the biological function of proteins (*42*). A few recent studies have applied PALM with endogenously tagged proteins (*43–46*). However, none of the studies could successfully quantify the number of proteins because of the challenges associated with the blinking behavior of PSFPs, which makes a single molecule appear multiple times (*29*) when blink correction (*32*) is not applied.

In this study, we have applied qPALM to analyze the oligomeric states and clustering behavior of endogenous ULK1 with single-molecule sensitivity. Endogenous ULK1 was expressed as a fusion with mEos3.2, one of the well-characterized PSFPs (*32, 47*), using CRISPR-Cas9–based genome editing (*48*). Under amino acid starvation, ULK1 assembled near the ER forming clusters comprising more than 30 ULK1 molecules. We found that this threshold number of ULK1 molecules is necessary for ULK1 clusters to participate in autophagosome formation. Through cross-correlation analysis, we determined that all structures containing more than 30 ULK1 molecules induced by starvation are associated with Atg13 and Atg14. These structures grew in size and were also associated with Atg16L1 (autophagy-related protein 16–like 1), LC3B [microtubule-associated proteins 1A/1B light chain 3B (MAP1LC3B)], GEC1 [glandular epithelial cell protein 1/gamma-aminobutyric acid receptor–associated protein-like 1 (GABARAPL1)], and WIPI2 (WD repeat domain phosphoinositide-interacting protein 2) for autophagosome maturation. We also determined distinct functions of ULK1 and Vps34 (vacuolar protein sorting 34 homolog) kinase activities in the initial clustering of ULK1 and the subsequent expansion of the clusters.

RESULTS

Quantitative analysis of endogenous ULK1 clusters reveals its high-order multimeric states

ULK1 forms puncta in the cytoplasm before autophagosome formation (*16, 17, 19*). To characterize the properties of ULK1 puncta, we used qPALM and quantified the multimeric states of ULK1 molecules. To avoid potential artifacts of qPALM analysis caused by overexpression (fig. S1), we engineered the genome of HeLa cells using the CRISPR-Cas9–assisted genome editing technique (*48*),

introducing mEos3.2 into the allele of the ULK1 gene (Fig. 1A). We then selected genome-edited cells that expressed all endogenous ULK1 molecules with mEos3.2 tagged at the N terminus (Fig. 1B). We confirmed that the endogenously tagged ULK1 forms functional complexes with Atg13 similar to untagged endogenous ULK1 (Fig. 1B). In response to amino acid starvation, the tagged ULK1 exhibited the same patterns of change in key phosphorylations as the untagged endogenous ULK1 (Fig. 1C). Specifically, amino acid starvation eliminated the phosphorylation of Ser^{758} by mTORC1 and the phosphorylation of Ser^{556} by AMPK (adenosine monophosphate protein kinase), both of which indicate suppression of ULK1 activity (*49*). Moreover, upon amino acid starvation, mEos3.2-tagged ULK1 was activated to phosphorylate Atg14 Ser^{29}, which is crucial for phagophore formation (*19*). The genome-edited cells also showed induction of Atg13 and LC3B puncta to a similar extent as unmodified HeLa cells under amino acid starvation (fig. S2). We further confirmed that the endogenous tagging does not affect autophagy flux of HeLa cells as reflected in the differences of LC3B II and p62 levels in the presence and absence of BAFA1 (bafilomycin A1), a lysosomal inhibitor (Fig. 1, D and E).

Using the genome-edited cells, we conducted PALM analysis of mEos3.2-ULK1 to determine the oligomeric states of ULK1. Each time a single mEos3.2 molecule was photoactivated and fluoresced, its center of mass was determined by a Gaussian fit to its intensity profile. Because mEos3.2, like other fluorophores, can emit a variable number of fluorescent burst that are separated by a variable short dark time, a single molecule can appear as a cloud of localizations in raw PALM data (*29*). To correct for these clustering artifacts, we used our previously developed method that groups localizations originating from the same mEos3.2 molecule to a single, photon-weighted averaged position based on a spatiotemporal threshold (see Methods and fig. S3) (*32*). By applying this blink correction, we obtained the detected number of ULK1 molecules in ULK1 clusters with ~25-nm resolution (fig. S3H) as well as the overall distribution of oligomeric states (Fig. 1F). It is important to note that not all mEos3.2 molecules are detectable, as demonstrated in previous studies using various model systems (*32, 33*) (see Methods). Throughout this paper, we only report the number of detected molecules for clarity.

Amino acid starvation induces high-order ULK1 oligomers

Regardless of amino acid presence or absence, mEos3.2-ULK1 was distributed throughout the whole cytoplasm of cells (Fig. 2A). Distinctly in amino acid–starved cells, we observed emerging arc-shaped and spherical structures of various sizes (Fig. 2A, right insets). These structures could not be resolved or discriminated in confocal fluorescence images. Via qPALM analysis, we grouped molecules appearing within a radial distance of 400 nm, the size that can encompass large structures induced by starvation up to a size of 800 nm (Fig. 2A, zooms, and Methods). In fed and starved conditions, the probability of finding monomeric ULK1 was 30%, with the remaining 70% being in higher-order oligomeric states. The probability of finding ULK1 clusters containing up to 10 molecules in either fed or starved conditions was 98% (Fig. 2B, inset), corresponding to a fraction of 93% of all ULK1 molecules in fed and 89% in starved cells. Starvation induced 5% of all ULK1 molecules to shift from lower to higher oligomeric states. In fed cells, the highest observed number of ULK1 molecules in a structure was 59, whereas in starved cells this number substantially increased to 144. It is
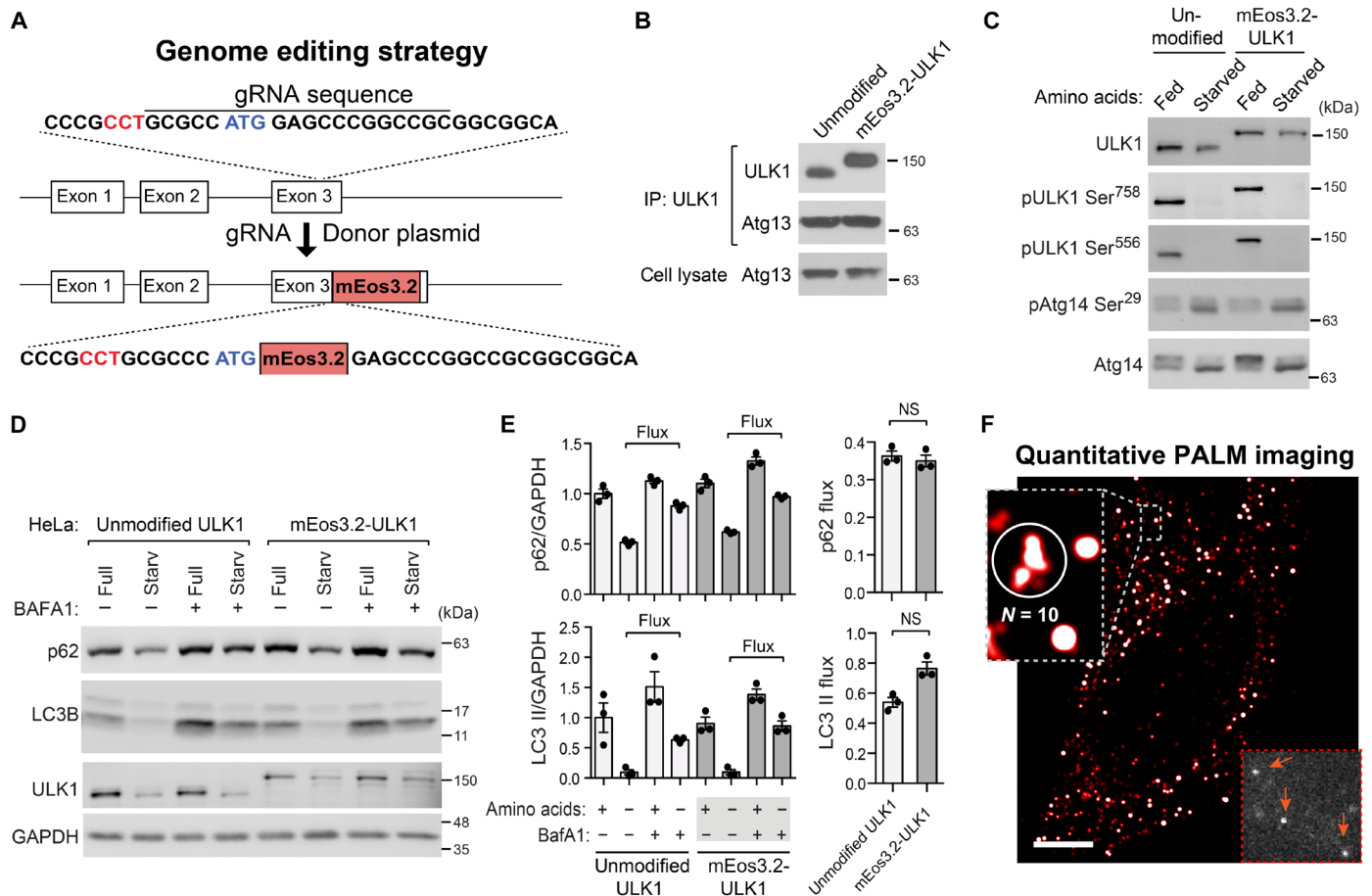
Fig. 1. Quantitative PALM reveals the nanoscopic distribution and oligomeric state of endogenous ULK1. (**A**) Schematics of endogenous tagging of ULK1 with mEos3.2. The gRNA PAM sequence is depicted in red. The detailed procedure is described in Methods. (**B**) The endogenously tagged ULK1 interacts with Atg13 to the same degree as the untagged endogenous ULK1. Immunoprecipitates were obtained from genome-modified HeLa cells (mEos3.2-ULK1) or unmodified HeLa cells grown in full medium using an anti-ULK1 antibody and analyzed by Western blotting for endogenous ULK1 and Atg13. (**C**) Endogenously tagged ULK1 is functionally intact for activation of ULK1 in response to amino acid starvation. Cells were incubated in amino acid–enriched full medium (fed) or amino acid–deprived medium (starved) for 60 min. The phosphorylation levels of ULK1 and Atg14 and their total protein levels were analyzed by Western blotting. (**D**) Autophagy flux, monitored by the levels of p62 and LC3B II using BAFA1, was similar in cells expressing unmodified ULK1 and in those expressing endogenously tagged mEos3.2-ULK1, as shown by Western blotting analysis. (**E**) Quantitative analysis of autophagy flux. The protein levels of p62 and LC3 II from (D) were quantified relative to glyceraldehyde-3-phosphate dehydrogenase (GAPDH) serving as a loading control. The levels in p62 flux and LC3 II flux were determined by comparing the amounts in the presence and absence of BAFA1. Data are shown as means ± SEM. Data were analyzed by two-tailed Student's t test. NS, not significant. (**F**) PALM image (red/white) showing the nanoscopic distribution and oligomeric state of ULK1 oligomers throughout the cytoplasm. Scale bar, 5 μm. The bottom right inset shows bright single-molecule fluorescence of mEos3.2-ULK1 in a single data acquisition frame. The zoom on the left exemplifies quantification of oligomeric state of a ULK1 cluster.

important to note that these highest-order oligomeric states occur with low probability and are thus not an accurate metric for comparison. Below, we have quantified with a high level of statistical confidence that the most significant increase in oligomeric states upon autophagy induction by starvation occurs when a threshold number of 30 ULK1 molecules is reached.

To further clarify how amino acid starvation affects ULK1 clusters, we conducted the pair correlation analysis. The pair correlation magnitude, which quantifies the density of molecules as a function of their intermolecular distance, exhibited a peak in starved and fed cells, indicating the accumulation of ULK1 compared to a random distribution. In starved cells, the pair correlation was significantly higher compared to fed cells at distances from 0 to 600 nm (Fig. 2C). While the absolute difference in the pair correlation magnitude appears to be small, it is important to note that only about 5% of all

ULK1 molecules are induced by starvation to form higher-order oligomers. This result corroborates the observation that amino acid starvation induces the formation of larger structures with denser ULK1 molecules (*17, 18*).

Starvation-induced structures with high numbers of ULK1 molecules form within 100 nm of the ER

It is known that autophagy initiation occurs on the surface of the ER (*11, 16*). To clarify whether our observed starvation-induced structures with a large number of ULK1 molecules form at the ER, we performed colocalization PALM analysis using mEos3.2-ULK1 HeLa cells transiently transduced with HaloTag-tagged Sec61β, an ER marker protein. The HaloTag protein covalently binds its ligands, each carrying an attached organic fluorophore, in a one-to-one ratio, producing high photon counts and thus high localization
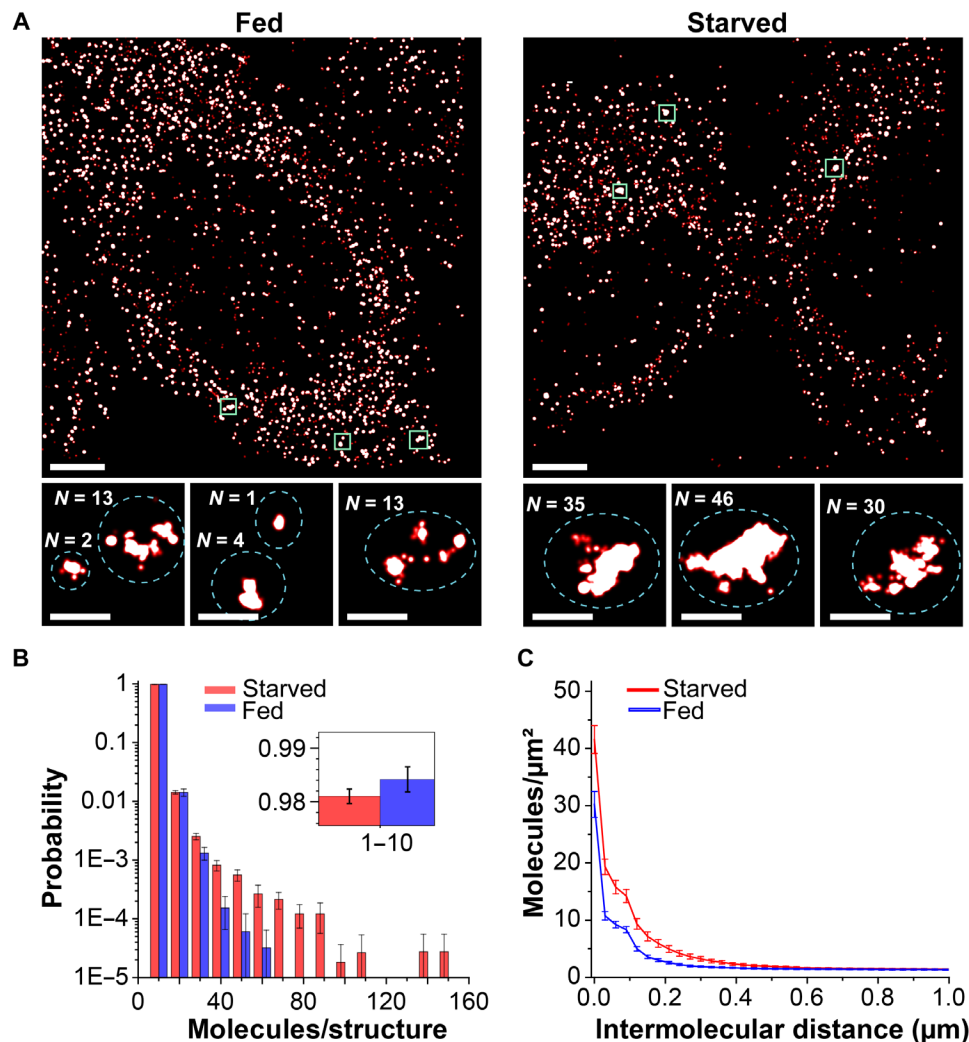
Fig. 2. Amino acid starvation induces clusters with more ULK1 molecules and larger size. (**A**) PALM images of mEos3.2-ULK1 in amino acid–supplemented cells (fed) and amino acid–deprived cells (starved) for 150 min. Scale bars, 5 μm. Magnified regions show small diffraction-limited structures, which were impossible to be resolved in conventional fluorescence images, and the corresponding number of ULK1 molecules. Scale bar, 500 nm. (**B**) The cluster analysis after the blink correction shows that amino acid starvation induced the formation of higher-order oligomers and structures containing up to 144 ULK1 molecules (red) compared to 59 ULK1 molecules observed in fed cells (blue). The inset shows the top of the first bin, highlighting that most ULK1 exists in oligomers consisting of 2 to 10 molecules. Error bars of each bin represent the SEM with a variance calculated from the cell-to-cell variability. (**C**) The pair correlation function of ULK1 in cells from (B) quantifies the molecular densities as a function of their intermolecular distances. A peak at short distances reflects the accumulation of molecules with respect to a random distribution. The statistically significant difference between starved (red) and fed cells (blue) at distances between 0 and 400 nm reflects an increase of cluster sizes and molecular densities upon starvation. Errors represent the SEM, which is calculated from the values of individual cells (fed: $N = 21$ cells, starved: $N = 34$ cells).

precision (*50*, *51*). To generate two-color PALM images, we used the JF646 fluorophore, which has no spectral overlap with mEos3.2. mEos3.2-ULK1 was localized not only on or near the tubular ER regions but also to some extent throughout the cytoplasm in both fed and starved cells (Fig. 3A). In starved cells, the induced structures with many ULK1 molecules were found in contact or close to the ER (Fig. 3A, lower right, and fig. S4). To determine the location of starvation-induced structures containing many ULK1 molecules with respect to the ER, we separately analyzed ULK1 molecules that appeared within a 100-nm distance from an ER localization (see Methods). In fed cells, the distribution of the number of ULK1 molecules and the radii of structures were similar whether they were in proximity to the ER or not (Fig. 3B, left). Only in starved cells, we

again observed structures with a large number of ULK1 molecules that occurred at the ER and were not present in fed cells.

To further visualize the distinct population of structures with a high oligomeric state of ULK1 at the ER, we created a normalized histogram of the number of ULK1 molecules in each structure (Fig. 3C). Structures located more than 100 nm away from the ER contained up to 38 ULK1 molecules, whereas structures within 100 nm proximity contained up to 122 ULK1 molecules. Therefore, starvation-induced structures that contain a high number of ULK1 molecules are located at and near the ER. This analysis cannot rule out the role of contact sites with other organelles. For instance, in fig. S5, we show that ULK1 as well as starvation-induced ULK1 structures are also associated with lysosomes. However, notably
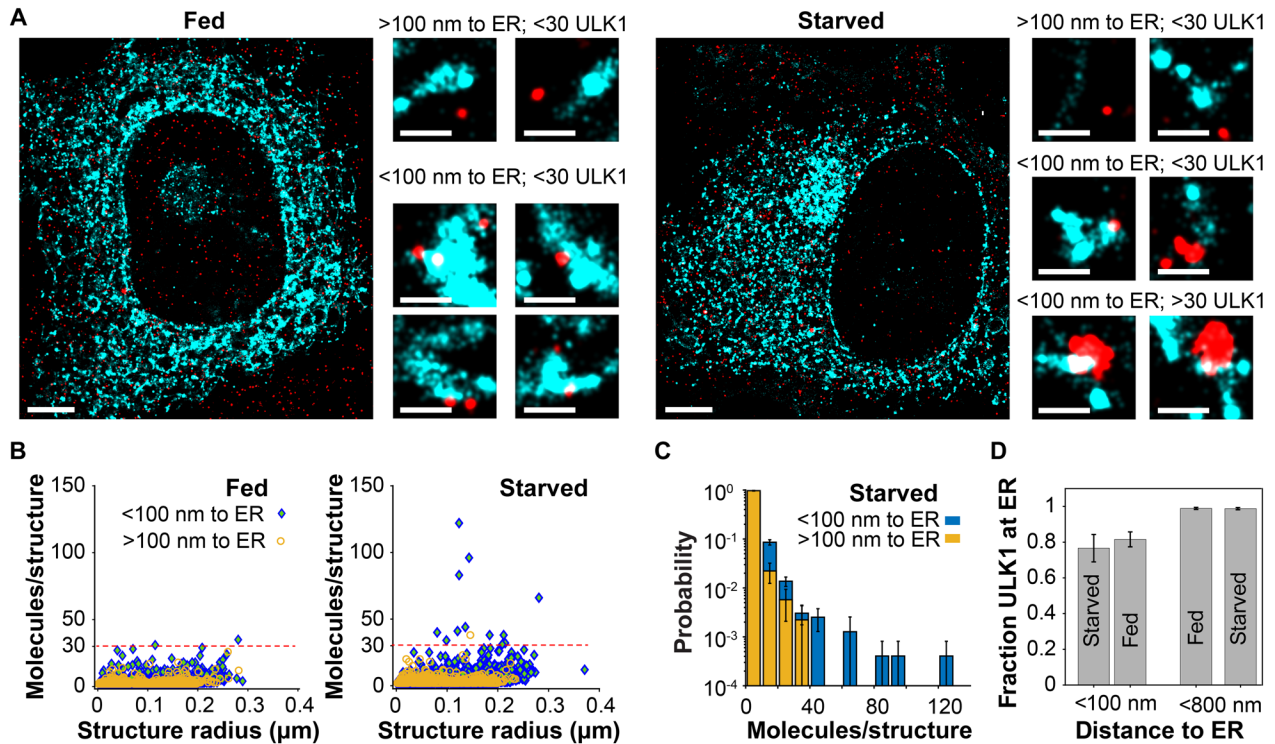
Fig. 3. Starvation-induced ULK1 structures are in proximity to the ER. (**A**) Two-color PALM images of mEos3.2-ULK1 (red) and the ER marker HaloTag-Sec61β (cyan) in fed (left) and starved cells (right). Zoom images of ULK1 and the ER show the presence of ULK1 clusters only on or near the ER in fed cells. In starved cells, larger ULK1 structures with more than 30 ULK1 molecules are in contact or in proximity to the ER (bottom right). Scale bars, 5 μm (main) and 1 μm (zoomed). (**B**) Quantification of the number of ULK1 molecules and the approximated radius of structures closer than 100 nm (blue) and further away from the ER (yellow) in fed and starved cells. Structures with a large number of ULK1 molecules that are later identified to contain Atg13 are only found in close proximity to the ER in starved cells. (**C**) Normalized histogram of the number of ULK1 molecules in structures of starved cells. Structures in proximity to the ER exhibit the highest number of ULK1 molecules. (**D**) Fraction of ULK1 molecules at a given distance from the ER in fed and starved cells. In both fed and starved cells, about 80% of all ULK1 molecules were within a distance of 100 nm from an ER localization, whereas more than 95% of ULK1 molecules were within a distance of 800 nm. Errors represent the SEM from four fed and five starved cells.

more structures are found away from lysosomes compared to the ER, demonstrating that their localization is more specific to the ER. In both fed and starved cells, about 80% of all ULK1 molecules were within a distance of 100 nm from the ER, whereas more than 95% of ULK1 molecules were within a distance of 800 nm (Fig. 3D). No significant difference of the ULK1 localization with respect to the ER was observed between fed and starved cells. These results suggest that ULK1 molecules engaging in autophagy are localized at and near the ER, where they accumulate to form larger structures with a large number of ULK1 molecules.

ULK1 structures containing Atg13 exhibit considerable variability in size, shape, and multimeric state

ULK1 interacts with Atg13 to regulate autophagy (5–7). We therefore wondered whether the higher-order multimeric states of ULK1 in starved cells are related to the autophagy initiation complex containing both ULK1 and Atg13. To address this, we performed colocalization PALM experiments monitoring both ULK1 and Atg13. We transiently expressed Atg13 as a fusion with HaloTag in the mEos3.2-ULK1 HeLa cells and treated the cells with the HaloTag dye ligand attached to JF646. In fed cells, both Atg13 and ULK1 formed small clusters that did or did not colocalize with each other throughout the cytoplasm (Fig. 4A, top). Starved cells also contained

small ULK1 clusters, many of which did not colocalize with Atg13. However, starvation induced large arc-shaped and spherical structures that contained both ULK1 and Atg13 (Fig. 4A, bottom, and fig. S6). These structures were not observed in fed cells. ULK1 structures associated with Atg13 exhibited a variety of sizes, shapes, and multimeric states. Some of the structures contained small dense ULK1 clusters, whereas some contained large ULK1 clusters with various oligomeric states (Fig. 4B). In contrast, ULK1 molecules that did not colocalize with Atg13 only formed small clusters (Fig. 4B, right). This colocalization PALM analysis showed that the clustering pattern is different between ULK1 structures that colocalized with Atg13 and those that did not colocalize with Atg13.

To further clarify the nature of ULK1 clusters that colocalize with Atg13, we performed cross-correlation analysis (39, 52) of ULK1 and Atg13. Like pair correlation analysis, cross-correlation analysis of two-color PALM data allows for robust quantification of the co-distribution of two different proteins (45, 52). When the two proteins are randomly distributed with respect to each other, the cross-correlation value becomes one. However, when two proteins interact and are more likely to colocalize within a short distance, the magnitude of the cross-correlation is larger than one up to that distance. Using the cross-correlation analysis, we measured the extent of colocalization between Atg13 and ULK1. In fed cells, we observed
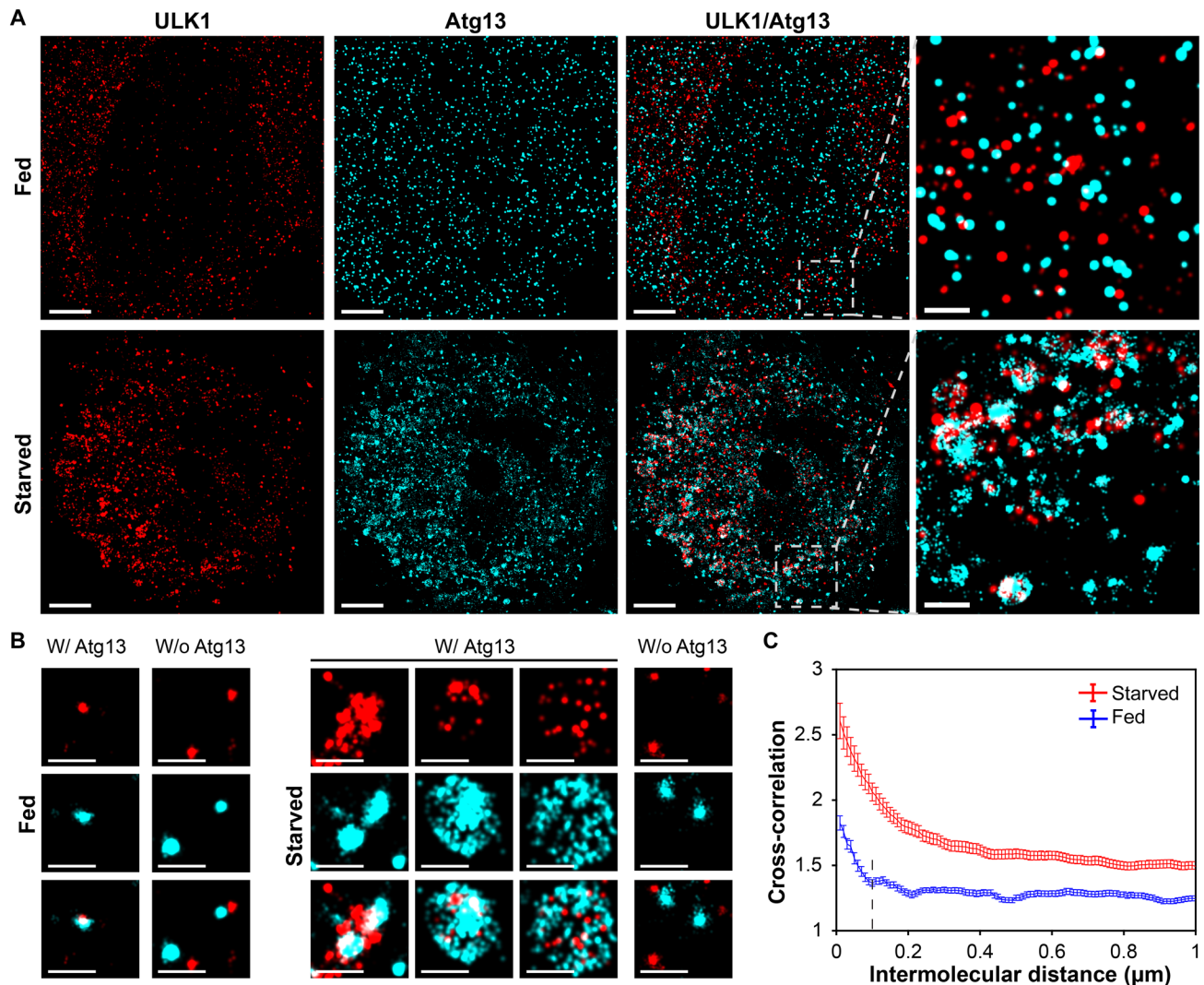
Fig. 4. ULK1 clusters containing Atg13 display variability in size, shape, and multimeric state under starvation. (**A**) Left: Two-color overlay of PALM images of mEos3.2-ULK1 (red) and HaloTag-Atg13 bound to JF646 (cyan) in fed (top) and starved cells (bottom). Scale bar, 5 μm. Right: Magnified images show the presence of various small dense ULK1 and Atg13 clusters that do or do not colocalize (top). Upon starvation, larger spherical and arc-shaped structures containing both Atg13 and ULK1 become visible (bottom). Scale bar, 1 μm. (**B**) Left: Examples of magnified two-color PALM images in fed cells show small ULK1 clusters that do not colocalize with Atg13. Right: In starved cells, Atg13 forms denser and larger arc-shaped or spherical structures that are associated with ULK1. ULK1 that does not contain Atg13 only forms small cluster. Scale bar, 500 nm. (**C**) Cross-correlation of ULK1 and Atg13 shows colocalization between ULK1 and Atg13 up to a distance of 100 nm in fed cells (blue) and a substantially larger degree of colocalization beyond 200 nm in starved cells (red). The error bar corresponds to SEM from 7 fed and 10 starved cells. Condition: 150 min of amino acid starvation with 180 nM BAFA1 to increase the number of detected autophagosomes in each cell by inhibiting the fusion of autophagosomes with lysosomes.

a peak of the cross-correlation at short distances up to 100 nm; however, under starvation, the peak was notably higher in a broad range of distance (Fig. 4C). This suggests a substantially increased level of colocalization between ULK1 and Atg13 within enlarged structures induced by starvation, which might be relevant to autophagosome formation. In our previous report (6), we used coimmunoprecipitation analysis to investigate the ULK1-Atg13 interaction in response to amino acid starvation, but no significant difference was detected. However, this method has limitations in capturing the dynamics of protein interactions in cells, as protein-protein interactions are often disrupted in vitro during the coimmunoprecipitation process. In contrast, our current study demonstrates, through colocalization

analysis, that ULK1 and Atg13 interact dynamically and form multimeric structures during the initiation of autophagy under amino acid starvation.

Starvation induces the formation of distinct Atg13-containing structures with more than 30 ULK1 molecules

To clarify which of the observed structures are involved in autophagy, we separately analyzed the ULK1 molecules that have a distance shorter than 100 nm to Atg13 (Atg13-bound structures) and those that have a distance longer than 100 nm (Atg13-free structures) (Fig. 5A and Methods). As in the previous quantification of the
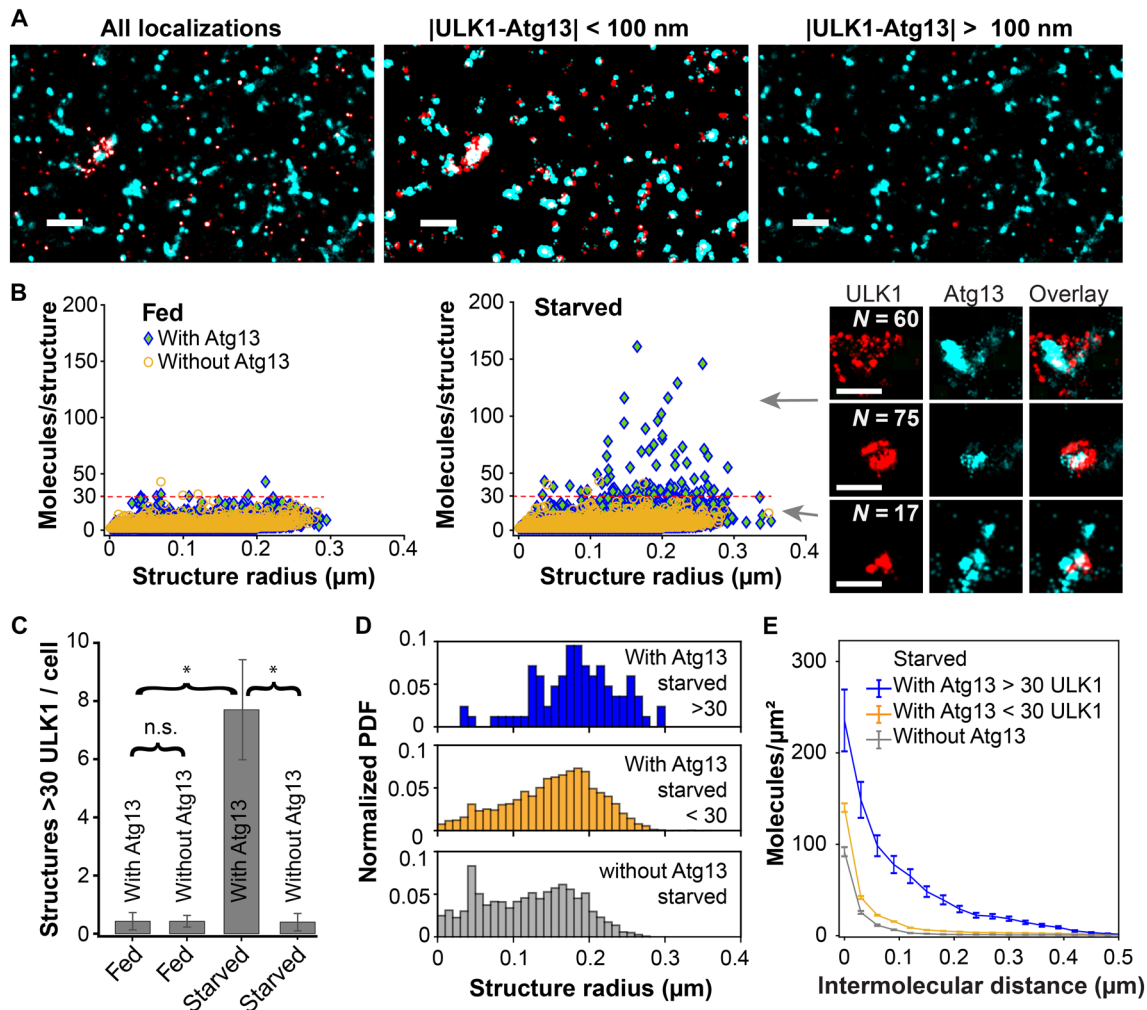
Fig. 5. Cross-correlation analysis of two-color PALM data identifies starvation-induced ULK1 structures containing Atg13 and more than 30 ULK1 molecules. (**A**) Left: Two-color PALM image of all mEos3.2-ULK1 (red) and Atg13-HaloTag JF646 (cyan) in starved cells. Middle: ULK1 molecules and clusters within 100 nm of Atg13 form highly dense and larger arc-shaped or spherical structures. Right: ULK1 further than 100 nm from Atg13 only forms small clusters. Scale bar, 1 μm. (**B**) Number of molecules and radii of ULK1-associated structures within a 100-nm distance of Atg13 (with Atg13, blue) and not in proximity to Atg13 (without Atg13, orange). Left: ULK1 structures exhibited similar distributions in fed cells regardless of Atg13-bound states. Middle: Small dense clusters and larger structures with more than 30 up to 161 ULK1 molecules form under starvation only when they contain Atg13 (dashed line: 30-molecule threshold for further analysis). Right: The inset images exemplify large Atg13-containing structures as well as a small dense cluster with less ULK1 molecules under starvation. Scale bar, 500 nm. (**C**) Number of structures with more than 30 ULK1 molecules per cell in different conditions. In fed cells, there was no significant difference, whereas a significant difference was present in starved cells [analysis of variance (ANOVA), $P = 0.05$]. Error bars are SEM. (**D**) Probability density function (PDF) of the radii of the three indicated types of structures. (**E**) Pair correlation quantifies the density of ULK1 molecules as a function of their distance on the three different types of ULK1 structures. Data were recorded from 7 fed and 10 starved cells. Condition: 150 min of amino acid starvation with 180 nM BAFA1 to increase the number of detected autophagosomes in each cell by inhibiting the fusion of autophagosomes with lysosomes.

oligomeric state of ULK1 in proximity to the ER (Fig. 3), we determined the number of ULK1 molecules in each structure and, in addition, approximated their radius (Fig. 5B and Methods). In fed cells, ULK1 showed similar distribution patterns regardless of Atg13-bound states with a maximum number of 43 ULK1 molecules (Fig. 5B). There was also no detectable difference in the radii of the two types of ULK1 structures. In contrast, amino acid starvation induced substantial differences between the two types of ULK1 structures. Atg13-free structures had no detectable difference in their number of ULK1 molecules and in their radii compared to fed

cells, whereas Atg13-bound structures contained significantly more ULK1 molecules up to 161 under starvation (Fig. 5B, right). By comparing the abundance of structures that have a large number of ULK1 molecules in fed and starved cells, we identified a threshold number of 30 ULK1 molecules. At this threshold, the difference in the distribution of the number of structures was most significant between fed and starved cells by various metrics (fig. S7). In short, if a lower threshold is set, the difference of Atg13-bound structures between starved and fed cells becomes smaller. If a larger threshold is set, the difference of Atg13-bound structures between starved and

fed cells also becomes smaller, and in addition, the number of structures in fed cells becomes too small and increases the statistical uncertainty of the comparison.

Starved cells had on average about seven to eight structures per cell that contained both Atg13 and more than 30 ULK1 molecules, which is an about 18-fold increase compared to fed cells (Fig. 5C). We used the lysosomal inhibitor BAFA1 only in these experiments to increase the statistics for an accurate determination of the threshold of 30 ULK1 molecules. The number of structures with more than 30 ULK1 molecules also significantly increased over time after starvation even in the absence of BAFA1 (fig. S8).

The normalized histogram of the radii of Atg13-free structures was roughly constant up to a radius of ~200 nm, whereas Atg13-bound structures showed different distributions depending on the number of ULK1 molecules (Fig. 5D). When Atg13-bound structures contained less than 30 ULK1 molecules, the radii spanned a broad range from the smallest measurable values up to 300 nm and exhibited a peak at approximately 200 nm (Fig. 5D). When Atg13-bound structures contained more than 30 ULK1 molecules, most radii were larger than 100 nm and radii up to 300 nm were detected. These results suggest that Atg13-bound structures with more than 30 ULK1 molecules tend to be larger compared to structures with less than 30 ULK1 molecules or structures without Atg13. To further characterize the density of ULK1 in these three classes of structures, we calculated the pair correlation function, which quantifies the average density of neighboring ULK1 molecules relative to each ULK1 molecule at a given distance. Atg13-free structures formed smallest clusters with a low ULK1 density, whereas Atg13-bound structures with less than 30 molecules had slightly higher density and size. In contrast, Atg13-bound structures with more than 30 ULK1 molecules formed the densest and by far the largest structures (Fig. 5E). All but one of these structures with more than 30 ULK1 molecules were located within a 100-nm distance from the ER as shown above (Fig. 3B, right, and fig. S4). We considered the possibility that transient expression of Atg13-HaloTag might affect the clustering behavior of ULK1 or its colocalization with Atg13. However, in fig. S9, we demonstrate that transient expression of Atg13-HaloTag does not change the clustering behavior of ULK1 or the colocalization of starvation-induced structures with Atg13.

In summary, our analysis identified unique starvation-induced structures that contained more than 30 ULK1 molecules as well as Atg13. These structures were not found in fed cells. While only about 4% of all ULK1 molecules were found in these structures in starved cells, the abundance of these structures in starved cells was significantly higher (~18-fold) compared to fed cells. ULK1 clusters that did not associate with Atg13 had a lower density and were smaller compared to Atg13-bound structures with more than 30 ULK1 molecules, which highlights the different state of ULK1 when associated with Atg13. We speculate that those Atg13-free ULK1 molecules might function in nonautophagic processes, such as ER-to-Golgi trafficking (53).

A colocalization map quantifies the association of ULK1 with other autophagy proteins

To further verify that our identified structures are autophagy specific, we applied the same colocalization analysis for Atg14, WIPI2, Atg16L1, GEC1, and LC3B, all of which play key roles in autophagosome formation. As in the experiments with Atg13, those proteins were expressed as a fusion with HaloTag. First, we quantified the number of structures per cell that contained more than 30 ULK1 molecules. In fed cells, either no or only a very small number of structures were detected regardless of the HaloTag-tagged autophagy proteins (Fig. 6A). Under starvation, a substantial number of structures per cell with more than 30 ULK1 molecules were detected and almost all these structures contained Atg14, WIPI2, Atg16L1, GEC1, and LC3B. This result further suggests that our identified structures with more than 30 ULK1 molecules are involved in the initiation and the formation of autophagosomes. While Atg14, Atg16L1, WIPI2, GEC1, and LC3B are known for their involvement in different stages of autophagosome formation, the single-molecule sensitivity of our experiments revealed their presence in stages where structures with more than 30 ULK1 exist.

To gain further insights into the nanoscopic distribution and degree of colocalization of ULK1 with those five proteins, we calculated the cross-correlation functions and quantified the peak amplitude above baseline as well as its width (Fig. 6B, fig. S10, and Methods). The cross-correlation magnitude above a value of 1 indicates the degree of colocalization, and the width of the cross-correlation peak indicates the average size of structures to which the two proteins localize. In fed cells, Atg16L1 and LC3B did not colocalize with ULK1 at all, whereas Atg14, WIPI2, and GEC1, like Atg13 (Fig. 5C), were to a small degree already colocalized with ULK1. Representative two-color PALM images and examples of starvation-induced structures are shown in Fig. 6C. This result suggests that Atg14, WIPI2, and GEC1 are, to some extent, preassembled with ULK1 in fed cells.

Upon starvation, all proteins except Atg14 strongly increased their colocalization with ULK1. In addition, the sizes of structures to which all proteins localized also increased under starvation (calculated from the width of the cross-correlation peak in fig. S10), consistent with the growth of autophagosomal structures. If autophagosomes form by continuous growth, as also shown by the increase of ULK1 structure sizes over time (fig. S8), the average size of structures might represent stages in their maturation. Consequently, we interpret that Atg13 and Atg14, which form the smallest structures, are involved in an earlier stage of autophagosome formation. WIPI2, GEC1, LC3B, and Atg16L1 form the largest structures, which suggests their association with a later stage of autophagosome formation. Some of these results can be compared to and are consistent with findings from previous conventional fluorescence microscopy studies (17, 18, 54). For instance, time-lapse microscopy revealed that Atg13 localizes with LC3B to omegasomes but dissociates earlier than LC3B (18). Consistent with this, our study showed, on average, smaller ULK1-Atg13 structures compared to ULK1-LC3B structures. Likewise, Atg14 was previously reported to participate early in phagophore formation before Atg16L1 and LC3B are involved (17, 18). Our study is in line with those reports, as we observed that ULK1-Atg14 structures were smaller than ULK1-Atg16L1 and ULK1-LC3B structures. When comparing the cross-correlation function of structures containing more and less than 30 ULK1 molecules, it becomes evident that the colocalization of ULK1 with all other proteins mostly occurs within starvation-induced structures containing more than 30 ULK1 molecules (fig. S10). This result further highlights the importance of our identified critical threshold number of 30 ULK1 molecules in the initiation and formation of autophagosomes. It also demonstrates that structures
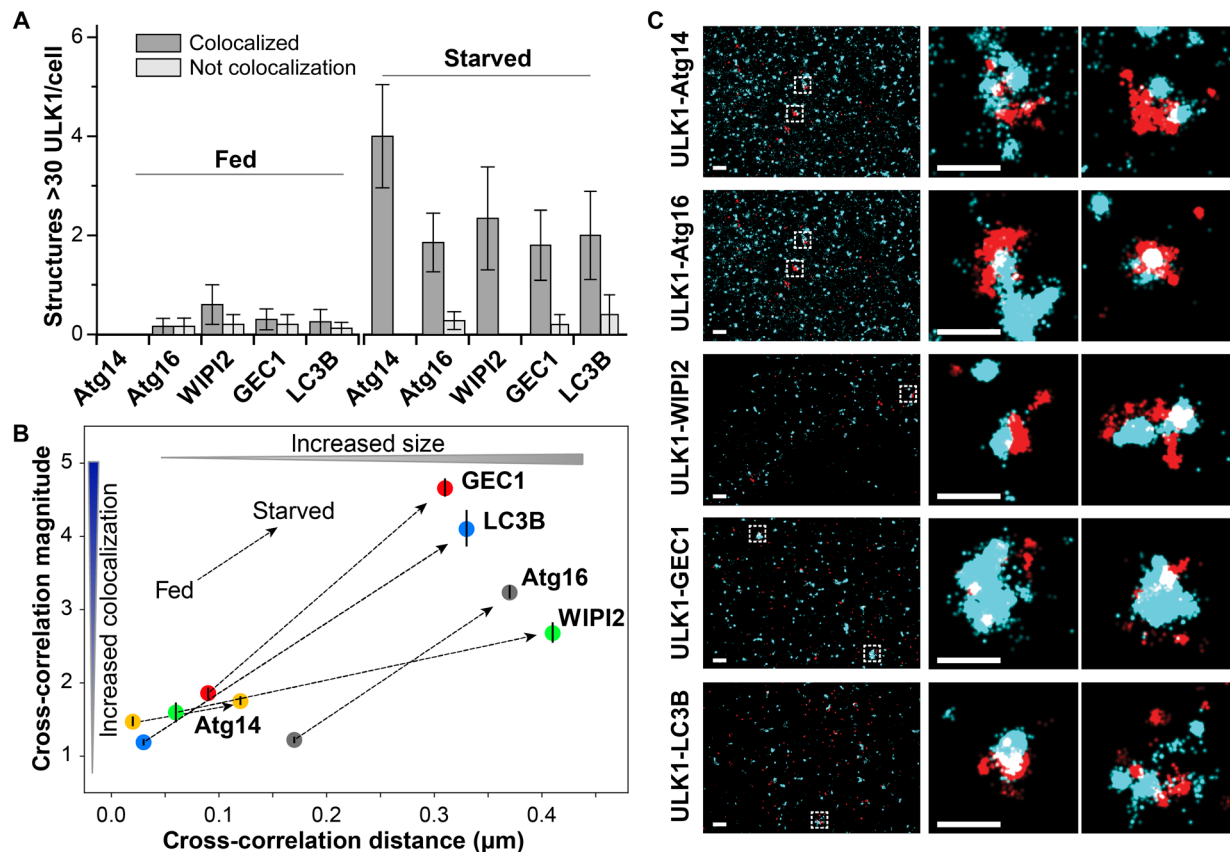
Fig. 6. Colocalization map of ULK1 with proteins involved in autophagy on starvation-induced structures. (**A**) Average number of structures per cell with more than 30 ULK1 proteins that do and do not colocalize with each indicated protein. Only upon starvation, a substantial number of structures with more than 30 ULK1 proteins are detected that colocalize with all proteins. (**B**) The cross-correlation magnitude of ULK1 with each indicated protein quantifies the degree of their overall colocalization with ULK1 in fed and starved conditions (value of 1 means no colocalization). The cross-correlation distance represents the average size of structures on which the colocalization occurs. Arrows connect the data points of each pair of proteins in fed and starved conditions. In fed cells, Atg16 and LC3B have no colocalization with ULK1, whereas Atg13, Atg14, WIPI2, and GEC1 are, to some extent, assembled in clusters with ULK1. All pairs of proteins exhibit a large increase in colocalization on starvation-induced structures with a significant increase in size. (**C**) Representative two-color PALM images under starvation and zooms that show starvation-induced structures with more than 30 ULK1 molecules (red) that colocalize with the other autophagy-related proteins (cyan). All data are recorded after 60 min of starvation.

with more than 30 ULK1 molecules are involved in all stages of autophagosome formation where those other autophagy proteins localize.

Vps34 and ULK1 kinase activities differentially affect ULK1 clustering during autophagy initiation

Having identified and characterized the starvation-induced structures, we wondered about the roles of Vps34 and ULK1 kinase activities in the formation of these structures. To assess the impact of Vps34 activity, we treated mEos3.2-ULK1 HeLa cells with the Vps34 inhibitor SAR405 (*55*), which has previously been shown to impede autophagy initiation and flux. When cells were starved in the presence of SAR405, the observed number of ULK1 structures per cell with more than 30 ULK1 molecules significantly decreased approximately fourfold (Fig. 7A) compared to starved cells without SAR405. This decrease was statistically similar to that observed in fed cells. The few detected clusters with more than 30 ULK1 molecules exhibited similar sizes in both the presence and absence of SAR405 (Fig. 7B). These results demonstrate that Vps34 activity is essential for the assembly of ULK1 structures with more than 30 molecules

that participate in autophagosome formation. Because autophagy flux is also blocked, as evidenced by the substantial reduction in the number of LC3B puncta per cell in the presence of SAR405 (Fig. 7C), these results highlight the importance of the critical threshold of ULK1 molecules for autophagy initiation.

Treating mEos3.2-ULK1 HeLa cells with the ULK1 inhibitor MRT68921 (*56*) significantly increased the number of ULK1 clusters having more than 30 molecules in starved cells (3.5 ± 0.4 compared to 9.5 ± 0.8 per cell) (Fig. 7D). However, the mean cluster radius in the presence of the inhibitor ($0.143\ \mu m$) was significantly smaller than that in the absence of the inhibitor ($0.175\ \mu m$) (Fig. 7E), which suggests that ULK1 kinase activity is required for the expansion and maturation of ULK1 clusters. This notion is corroborated by the suppressive effect of ULK1 inhibition on LC3B puncta formation (Fig. 7F) as well as the increase of ULK1 structure sizes over time after starvation in the absence of the ULK1 inhibitor (fig. S8).

To clarify whether ULK1 inhibition affects not only the growth but also the colocalization of other autophagy-related proteins, we performed PALM colocalization analysis between ULK1 and other autophagy proteins (Atg14, Atg16L1, WIPI2, GEC1, and LC3B) in
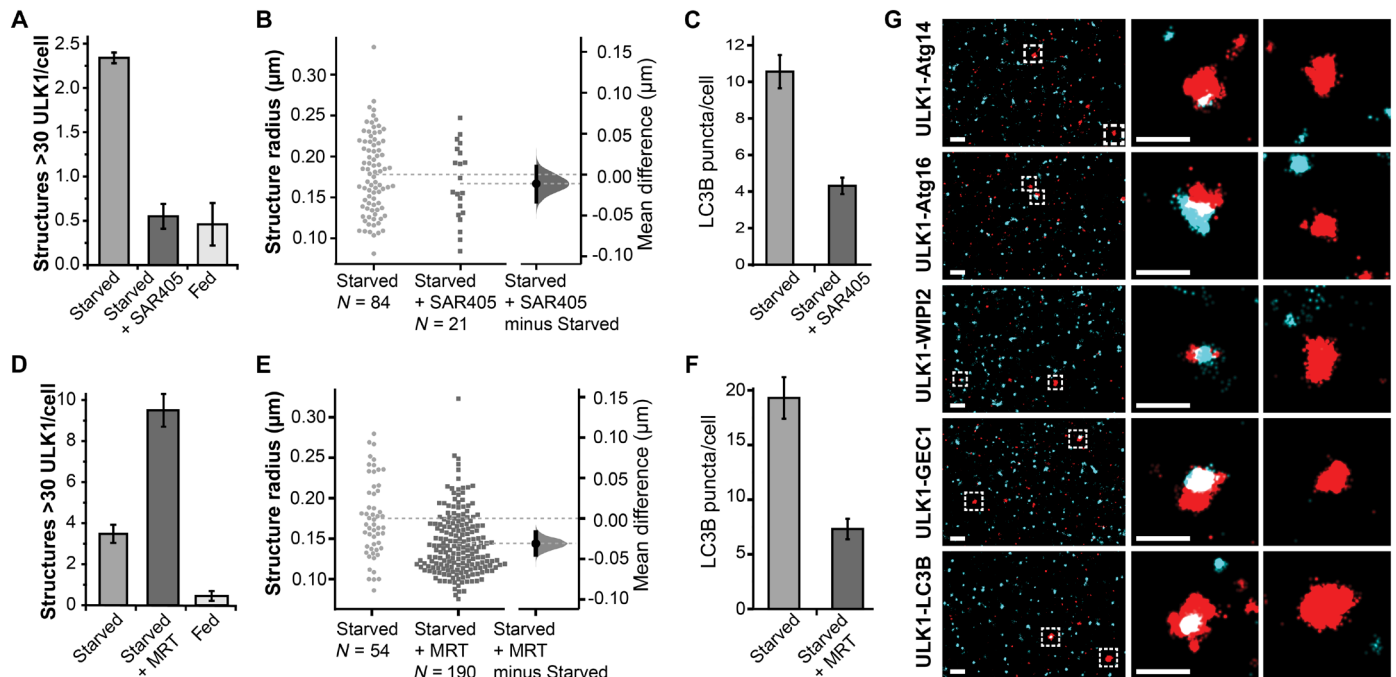
Fig. 7. Vps34 activity is required to assemble starved-induced ULK1 structures; ULK1 kinase activity is required for the expansion and maturation of ULK1 clusters. (**A**) The number of structures with more than 30 ULK1 per cell is significantly decreased in starved cells in the presence of the Vps34 inhibitor SAR405 (1 μM) and indistinguishable from fed cells (fed: $N = 20$, starved: $N = 35$, starved + SAR405: $N = 38$ cells, 150-min starvation). (**B**) These structures have no significant difference in size in the presence and absence of the Vps34 inhibitor. (**C**) Autophagy flux quantified by the number of LC3B-GFP puncta per cell is decreased in starved cells in the presence of SAR405 ($N = 30$ cells for each condition). (**D**) The number of structures with more than 30 ULK1 per cell is significantly increased in starved cells in the presence of the ULK1 inhibitor MRT68921 (1 μM) for 1 hour (fed: $N = 20$, starved: $N = 15$, starved + MRT68921: $N = 20$ cells, 60-min starvation). (**E**) The size of these structures is significantly smaller in starved cells in the presence of the ULK1 inhibitor (Mann-Whitney, $P = 1.2 \times 10^{-5}$ from 5000 bootstrap resamplings; ANOVA, $P = 1.2 \times 10^{-6}$). (**F**) Autophagy flux quantified by the number of LC3B-GFP puncta per cell is decreased in starved cells in the presence of MRT68921 ($N = 30$ cells for each condition). MRT68921 was added to fed cells for 30 min, and then cells were starved in amino acid–deficient medium in the presence of the inhibitor for 60 min. (**G**) Representative two-color PALM images (left) and zooms of individual structures with more than 30 ULK1 molecules (right) that do and do not colocalize with other autophagy-related proteins in the presence of the ULK1 inhibitor in starved cells (red, ULK1; cyan, other proteins).

starved cells in the presence of MRT68921. As expected, the total number of structures with more than 30 ULK1 molecules was again substantially larger in the presence of the ULK1 inhibitor with some variability between the different autophagy proteins due to a limited sample size and cell-to-cell variability. However, a significantly larger number of the structures with more than 30 ULK1 molecules did not contain the other autophagy proteins compared to starved cells without the ULK1 inhibitor (Figs. 6A and 8A). The most pronounced effect was observed for Atg14, Atg16L1, and LC3B. We also analyzed the radii of HaloTag localizations from the different autophagy proteins within the ULK1 structures, and compared the measurements to those in starved cells in the absence of the ULK1 inhibitor (Fig. 8B). In all cases, the ULK1 inhibitor significantly reduced the sizes of the structures. When comparing the cross-correlation between ULK1 and the other proteins in starved cells in the presence of the inhibitor, no colocalization was detected in structures containing fewer than 30 ULK1 molecules, similar to what was observed in the absence of the inhibitor (fig. S10). In structures with more than 30 ULK1 molecules, reduced colocalization was observed for all the autophagy proteins except GEC1, which unexpectedly exhibited a dramatic increase in colocalization. This could be due to the coincidental large number of observed structures with more than 30 ULK1 molecules per cell (Fig. 8A), or

to an unknown mechanism by which ULK1 activity weakens its association with GEC1.

These findings demonstrate that autophagosomal structures with more than 30 ULK1 molecules become stalled when ULK1 is inhibited, resulting in significantly smaller sizes and the inability to recruit Atg14, Atg16, WIPI2, and LC3B. ULK1 kinase activity is therefore required for the recruitment of those autophagy regulators and for the progression and expansion of early autophagosomal structures. These results are consistent with previous studies, which have shown that ULK1 inhibition led to the accumulation of stalled early autophagosomal structures (Fig. 8C) (*56*, *57*). Those studies also support our finding that ULK1 is involved not only in the induction of autophagy but also in the expansion and growth of early autophagosomal structures.

DISCUSSION
In this study, we have applied qPALM to quantitatively analyze the oligomeric state and the nanoscopic spatial distribution of ULK1 during autophagy initiation. By counting the number of ULK1 molecules in clusters, we found that more than 98% of ULK1 clusters (accounting for 93% of ULK1 molecules in fed cells and 89% in starved cells) contain 10 or less ULK1 molecules. Starvation induced
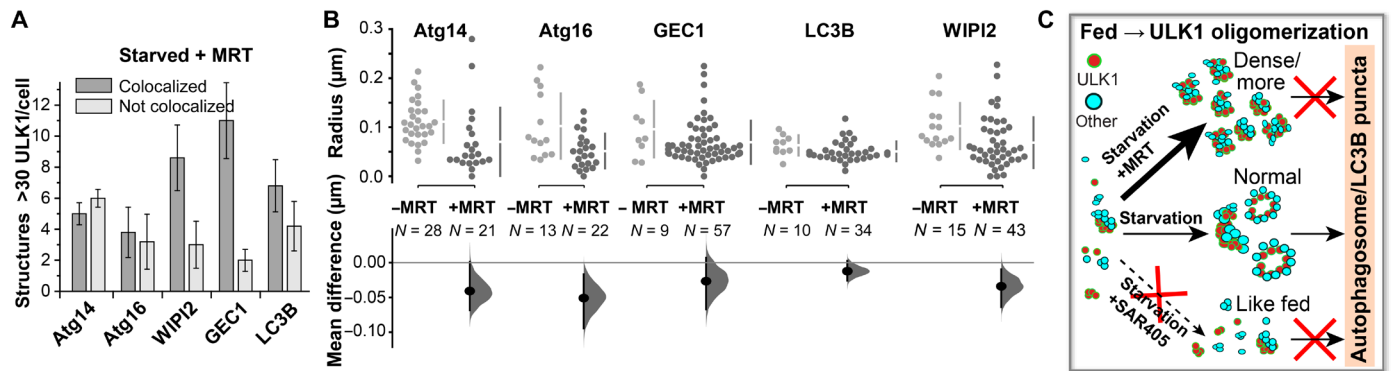
Fig. 8. The colocalization and size of starvation-induced ULK1 structures are disrupted upon ULK1 inhibition. (**A**) Average number of structures per cell with more than 30 ULK1 proteins that do and do not colocalize with each indicated protein in starved cells treated with MRT68921. Substantially more structures do not colocalize with autophagy-related proteins compared to starved cells in the absence of the ULK1 inhibitor (*N* = 5 to 8 cells for each condition, 60-min starvation). (**B**) The radii of these structures measured with HaloTag localizations from each autophagy protein in starved cells are significantly smaller in the presence of MRT68921. (**C**) Schematics of ULK1 cluster formation, association with other autophagy proteins, and progression to autophagosomes for the three different conditions.

about 5% of all ULK1 molecules to transition into higher-order oligomeric clusters and larger structures with a significantly increased number of ULK1 molecules compared to fed cells. A small fraction of these structures contained a large number up to 161 ULK1 molecules. Only during starvation, ULK1 formed small dense clusters as well as arc-shaped and spherical structures with more than 30 ULK1 molecules that colocalized with Atg13 (Figs. 2, 4, and 5). The statistically most significant difference in the number of ULK1 molecules in clusters between fed and starved cells was 30. We therefore propose that a minimal threshold of 30 ULK1 molecules must assemble to initiate and form autophagosomal structures.

Our quantitative PALM experiments achieved single-molecule sensitivity with a spatial resolution of about 25 nm. Although qPALM has been improved since its first development, the ability to quantify the number of molecules has remained limited. One approach for qPALM is to group localizations from the same fluorophore within a spatiotemporal threshold (*32, 33, 58*). A challenge for this quantification is that PSFPs do not emit at a constant intensity but rather exhibit a variable number of fluorescent bursts separated by a variable time. This phenomenon causes single PSFPs to appear as clusters with a variable number of localizations (*32, 39, 59, 60*). To quantify the oligomeric states of a protein, the PSFP must irreversibly bleach within a short timeframe relative to the entire imaging sequence. The distribution of dark times between fluorescent bursts of single PSFPs must also be determined. Because the photophysical properties of PSFPs depend on the experimental conditions, we determined both spatial and temporal thresholds for grouping localizations under our experimental condition. By performing PALM experiments at a very low photoactivation power to avoid spatiotemporal overlap of PSFPs, we determined a dark-time cutoff of 4.5 s, which correctly grouped localizations from more than 99% of ULK1 molecules (fig. S3). In addition, we analyzed endogenously tagged ULK1 to avoid any artifacts resulting from overexpression. If a pair of PSFPs suitable for molecule counting becomes available, we could expand our study by endogenously tagging the other autophagy proteins in conjunction with ULK1. This would allow us to characterize their oligomeric states and explore how they relate to ULK1.

Our two-color colocalization qPALM analysis also revealed that ULK1 molecules in fed and starved cells are predominantly localized on or in proximity to the ER. While this aligns with the broadly accepted notion that autophagosomes begin forming at the ER membrane (*18, 61*), our study is unique in demonstrating the dynamic alteration of ULK1 oligomeric states during the initiation process in the proximity of the ER membrane. Among the different forms of ULK1 structures, those induced by starvation and containing >30 ULK1 molecules were consistently and almost exclusively found on or near the ER (Fig. 3). Nevertheless, we do not exclude the possibility that other organelles, such as mitochondria, might have interactions with those ULK1 structures.

The arc-shaped and spherical structures of ULK1, which are induced by starvation and contain more than 30 ULK1 molecules, may resemble the early phagophore structures that were described in a recent study by Karanasios *et al.* (*16*). The arc-shaped structures might emerge from dense, small clusters comprising both ULK1 and Atg13 and subsequently expand into larger spherical structures. These structures with more than 30 ULK1 molecules also colocalized with Atg14, Atg16L1, WIPI2, GEC1, and LC3B, which are all well-known contributors to autophagosome formation. These proteins exclusively colocalized with the structures containing more than 30 ULK1 molecules, highlighting the importance of this threshold number. Assuming a continuous growth of autophagosomes, the average size of these structures may represent different stages in their maturation, which is also consistent with our observed increase in their size after starvation (fig. S8) and the enlargement of the structures colocalizing with other autophagy proteins (Figs. 5 and 6 and fig. S10).

The determination of the critical number of ULK1 molecules has also provided insights into the roles of ULK1 and Vps34 kinase activities in autophagy initiation. Inhibiting Vps34 kinase activity prevented the assembly of ULK1 clusters containing more than 30 molecules. In contrast, inhibiting ULK1 kinase activity resulted in an increased number of stalled autophagosomal structures with more than 30 ULK1 molecules (Fig. 7J). These results highlight the intricacies of autophagy initiation regulation at the level of ULK1 clustering. ULK1 activity influences the expansion of autophagosomal structures, whereas Vps34 activity regulates ULK1 clustering that is crucial for the initiation of autophagosome formation. ULK1 inhibition significantly increased the number of structures with

more than 30 ULK1 molecules in starved cells. These ULK1 clusters were smaller in size compared to those in starved cells without ULK1 inhibition, and did not contain other autophagy-related proteins to the same extent as observed in cells without inhibitor. This result is consistent with a recent report by Zachari *et al.* (*57*), where ULK1 inhibition was shown not to impede the formation of ULK1 puncta in starved cells. This indicates that ULK1 kinase activity is not required for assembling the critical number of 30 ULK1 molecules into an autophagy initiation complex, but rather plays a role in driving the expansion and progression of early ULK1 structures into autophagosomes.

Although our study has provided unprecedented insights into the nature and the behavior of ULK1 molecules during the initiation of autophagosome formation, it remains to understand the molecular mechanisms for how such large ULK1 clusters form and dynamically change their multimeric state and morphology. The mechanisms may involve posttranslational modifications, such as phosphorylation and acetylation, as well as protein-protein interactions. Combining single-molecule qPALM analysis with biochemical techniques may hold the potential to achieve a more comprehensive understanding of the complex mechanisms underlying autophagy initiation.

METHODS

Generation of genome-edited cells
To introduce the mEos3.2 tag into the *ULK1* gene locus of the genome of HeLa cells, we used the CRISPR-Cas9–assisted genome editing technique (*62*). The detail of the general procedure has been described in our previous report (*63*). The guide RNA (gRNA) sequence (GCGGCCGGGCTCCATGGCGC) was cloned into pSpCas9(BB)-2A–green fluorescent protein (GFP) (Addgene, PX458; deposited by F. Zhang). The replacement DNA was designed to contain 700 base pairs of the homologous region for both sides of the inserted mEos3.2 sequence. Four tandem repeats of GGT nucleotide sequences were added to the end of the mEos3.2 sequence. The gRNA plasmid and the replacement plasmid were introduced into HeLa cells using the Neon Transfection System (Thermo Fisher Scientific). GFP-positive cells were sorted and plated in 96-well plates as a single cell. Individual clones were screened for expression of mEos3.2-ULK1 by Western blotting and confirmed by genomic DNA sequencing.

DNA constructs, stable cell generation, and transient transfection
The full-length complementary DNAs (cDNAs) for Atg13, Atg14, GEC1, and LC3B were described in our previous reports (*6, 19, 64*). The cDNA clones for Sec61β (#49155) and Tmem192 (#102930) were obtained from Addgene, whereas the cDNA clones for Atg16L1 (BC013411) and WIPI2 (BC021200) were obtained from Open Biosystems (Huntsville, AL). The cDNA clones were amplified by polymerase chain reaction and subcloned into pLV-EF1a-IRES plasmid-blast vector (Addgene, #85133), which we further engineered to introduce the HaloTag sequence for N-terminal tagging. To stably introduce the plasmids into the genome-edited mEos3.2-ULK1 HeLa cells, we prepared the lentivirus. The procedures for lentivirus preparation and target cell infection have been described in our previous report (*6*). Briefly, lentivirus was prepared by transfecting human embryonic kidney (HEK) 293FT cells (Thermo Fisher Scientific, R70007) with each of the plasmids prepared as above

together with pHR′8.2DR and pCMV-VSV-G DNAs using Lipofectamine 3000 (Life Technologies Scientific, L3000015) at a 1:1:1 ratio. The culture medium containing the virus was collected 48 to 60 hours after transfection and filtered through a 0.45-μm syringe filter (Genesee Scientific, 25-245). The target cells (mEos3.2-ULK1 HeLa) were infected with the collected viruses in the presence of polybrene (Sigma-Aldrich, 107689). Stably transduced cells were selected in the presence of blasticidin (8 to 10 μg/ml). For HaloTag-tagged Atg13 and GFP-LC3B, we transfected mEos3.2-ULK1 HeLa cells with prk5-HaloTag-Atg13 and pLV-mGFP-LC3B DNA using GeneJET (Thermo Fisher Scientific). Twenty-four hours after transfection, cells were used for imaging.

Coimmunoprecipitation and Western blotting
The mEos3.2-tagged endogenous ULK1 was enriched by immunoprecipitation using an anti-ULK1 antibody (Santa Cruz Biotechnology, sc-10900) following the procedure we described in our previous report (*6, 19, 63*). We used a lysis buffer containing 40 mM Hepes (pH 7.4), 120 mM NaCl, 1 mM EDTA, 50 mM NaF, 1.5 mM Na$_3$VO$_4$, 10 mM β-glycerophosphate, and 1% Triton X-100 (Sigma-Aldrich, X100) supplemented with protease inhibitors (Roche, 05056489001). Immunoprecipitated proteins were run on tris-glycine gels (Thermo Fisher Scientific, XP04125), transferred onto immunoblot polyvinylidene difluoride membranes (Bio-Rad, 1620177), and detected using enhanced chemiluminescence reagents (GenDEPOT, 20-300B). The following antibodies were used for Western blotting: ULK1 (sc-33182) from Santa Cruz Biotechnology and p-ULK1 Ser[556] (#5869), p-ULK1 Ser[758] (#6888), p-Atg14 Ser[29] (#13155), and Atg14 (#96752) from Cell Signaling Technology; Atg13 antibody was described in our previous report (*6*).

Autophagy induction and flux analysis
For induction of autophagy, cells were incubated in Earle's balanced salt solution (EBSS) (Sigma-Aldrich, 2888) supplemented with 10% dialyzed fetal bovine serum (Thermo Fisher Scientific, 26400044) for an indicated duration. For autophagy flux analysis by Western blotting, cells were incubated in full medium or EBSS medium supplemented with serum in the presence or absence of BAFA1 (180 nM). LC3B and p62 in cell lysate were analyzed by Western blotting using antibodies from Cell Signaling Inc. (LC3B: 2775) and Santa Cruz Biotechnology (p62: sc-28359).

Preparation of cells for imaging
HeLa cells were maintained in fluorobrite Dulbecco's modified Eagle's medium (Gibco cat. #A1896701) supplemented with 10% fetal bovine serum, 4 mM glutamine (Gibco cat. #10437028), 1 mM sodium pyruvate (Gibco cat #11360070), and 1% penicillin-streptomycin antibiotics (Gibvo cat. #15140122) in a T25 flask. Cells were subcultured on eight-well chambered cover glasses (Cellvis, C8-1.58-N) 24 hours before transfection or imaging. All the imaging experiments have been performed in fixed cells. For fixation, cells were treated with 3% (v/v) formaldehyde for 30 min. After fixation, we used Dulbecco's phosphate-buffered saline (PBS) with calcium and magnesium (Gibco cat. #14040117) for measurements. For two-color PALM imaging of mEos3.2-ULK1 with Atg13-HaloTag, the ER marker Sec61-HaloTag, or other HaloTag protein fusions, we used the organic dye JF646 to stain HaloTag-tagged proteins (Promega cat. #GA1120). For conventional imaging of Atg13

(fig. S2), Oregon green (OG, Promega cat. #G2801) was used. Both dyes exhibit no overlap of their absorption and emission spectra with photoconverted mEos3.2. The dyes were added to live cells on the coverglass of the eight-well chambers at a final concentration of 500 nM for OG and 1 to 10 nM for JF646. Cells were incubated for 15 to 20 min and then fixed with 3% formaldehyde and washed five times with PBS containing 1% Triton X-100 to remove excess dyes.

PALM and conventional fluorescence data acquisition
All microscopy experiments were performed with a Nikon Ti-E inverted microscope with the Perfect Focus System and recorded on an electron-multiplying charge-coupled device camera (Ixon89Ultra DU897U, Andor) at a frame rate of 20 Hz as described in detail in the Supplementary Materials. In short, for PALM imaging of mEos3.2-ULK1, one photoactivation frame (405-nm laser, 1 to 251 μW corresponding to a power density of roughly 0.06 to 15 W/cm^2) with simultaneous transmitted light imaging was followed by nine frames of excitation (561 nm, 17 mW corresponding to a power density of roughly 1 kW/cm^2). For two-color PALM imaging of mEos3.2-ULK1 and HaloTag JF646, the excitation frames consisted of five 561-nm excitation frames for mEos3.2 followed by five 640-nm excitation frames (640 nm, 17.5 mW, roughly 1 kW/cm^2). Photoactivation and excitation cycles were repeated until all mEos3.2/JF646 molecules were imaged and bleached typically until a movie recorded at 20 Hz reached 8000 to 15,000 frames. The point spread functions of single molecules were then fitted with an elliptical Gaussian function using Insight3 (Zhuang laboratory, http://zhuang.harvard.edu/software.html) to determine their centroid positions, intensities, widths, and ellipticities. For all localizations, the x and y coordinates, photon number, background photons, width, the frame of appearance, and other fit parameters were saved in a molecule list for further analysis. To correct for drift, all molecule lists were drift-corrected using the repetitive transmitted light images (65). The conventional fluorescence images in fig. S2 were generated by averaging the 50 frames recorded at 20 Hz with a 488-nm excitation power density of 0.085 W/cm^2. Quantification of GFP puncta per cell was achieved with Insight3 in the same way as single-molecule fluorescence was quantified. Parameters for Gaussian fits in Insight3 were optimized on the basis of the sizes and intensities of puncta and consistently applied to all cells.

Quantitative analysis of molecule numbers
Once a single mEos3.2 molecule is stochastically photoactivated, it emits a variable number of fluorescent bursts that are separated by a variable dark time until irreversible bleaching occurs. These fluorescent bursts can be combined because the 405-nm photoactivation rate was kept low enough to avoid spatiotemporal overlap with a nearby mEos3.2 molecule. The combination of these fluorescent bursts is based on two thresholds: (i) a distance threshold that specifies the maximum separation of fluorescent bursts from a mEos3.2 molecule (corresponding to the localization precision) and (ii) a temporal dark-time threshold that specifies the maximum time between fluorescent bursts from a mEos3.2 molecule. The distance threshold was measured using the pair correlation function (fig. S3D), which revealed that fluorescent bursts from single mEos3.2 molecules are spatially separated by less than 80 nm. The dark-time threshold was determined from the cumulative dark-time histogram of fluorescent bursts and set to 4.5 s, which covers 99% of the dark times (fig. S3, E and F). On the basis of these two parameters, a

custom-written MATLAB procedure combines two localizations from fluorescent bursts to a photon-weighted average position if they are separated by less than 80 nm and less than 4.5 s. If a third localization again appears within the cutoff time with respect to the preceding one and within 80 nm compared to the averaged position of the previous two localizations, a new photon-weighted average position is calculated from the three localizations. This iterative process is repeated until all localizations from the same mEos3.2 molecules are combined to a photon-weighted average position. The average position has a higher localization precision due to the increased number of photons. From the resulting blink-corrected molecule list, the detected number of mEos3.2 molecules and their spatial distribution can be further analyzed. It is important to note that only about 40% of mEos3.2 molecules are detectable as identified by previous studies in different model systems (33). Thus, the actual number of molecules equals the detected number divided by 0.6. Throughout this manuscript, we only report the number of detected molecules for clarity.

To count the number of ULK1 molecules in initiation complexes and forming autophagosomal structures in an unbiased way, we determined their size distribution in the amino acid–starved conditions using the pair correlation function of the blink-corrected mEos3.2 molecule list (Fig. 2C). The pair correlation function g(r) was above 1 outside the experimental error (SEM) up to a distance of 800 nm, indicating accumulation of ULK1 molecules beyond a random distribution. Therefore, ULK1 molecules within a radius of 400 nm were assigned to one structure or cluster. Structures and clusters with a certain number of ULK1 molecules were then accumulated in a histogram with bin width 10.

Alignment of two-color PALM data
To superimpose two-color PALM data for images or cross-correlation analysis, we recorded conventional fluorescence images of fluorescent beads (TetraSpeck microspheres, Invitrogen T7279) that were excited at 561 and 640 nm and appeared in both channels. The transformation between the two channels across the field of view was then obtained by localizing individual beads in both channels and by determining the third-order polynomial transformation between their coordinates. The accuracy of the transformation was then verified by recording different fields of view of fluorescent beads and superimposing both channels using the determined transformation. As seen in fig. S11, the deviation of the bead locations from both channels was less than 19 nm, which is smaller than the localization precision of PALM.

Spatial cross-correlation analysis and cluster identification
After identification of blink-corrected ULK1 molecules, molecules were assigned to clusters. The radial distribution (or pair correlation) among all blink-corrected molecules was calculated, and molecules that were within 400 nm of each other were identified as ULK1 clusters. The obtained partial radial distribution function was normalized by the number of molecules in both datasets and the area of the field of view (39). Next, a spatial cross-correlation between the blink-corrected ULK1 molecules and localizations from the second protein of interest was performed to determine the distance distribution between the two proteins. Because of the large number of localizations in both the blink-corrected ULK1 and the Atg13 localization datasets, we set a 2-μm cutoff in the nearest neighbor search, which only requires 10 to 30 GB of working memory. This

method allows for the identification of molecule pairs within a specified distance distribution across the entire desired field of view for many movies using available computational resources (analysis code was written in MATLAB 2018b and run on an Alienware Aurora G6 computer with 3.80 GHz CPU, 40 GB of working memory, NVIDIA GeForce GTX 1070 8 GB graphics card, and 900 GB of disk space). Next, ULK1 clusters that contained at least one ULK1 molecule within 100 nm of a localization from the second protein of interest (labeled "with") were segregated from ULK1 clusters with no molecules within 100 nm of an Atg13 localization (labeled "without"). Cluster properties such as the radius and the number of ULK1 molecules were determined separately for a comparison of fed and starved cells. This cross-correlation analysis was also applied to ULK1 molecules and ER localizations. A detailed description of this analysis as well as the code can be found in (66).

Estimating radii of structures
To estimate the radius of the ULK1 clusters, the x and y positions of the molecules inside the cluster were averaged to find the center, and the distance between each molecule and the center was calculated. The mean of the distances from the center was then used to approximate the radius of the ULK1 cluster.

Cross-correlation distance and magnitude
The height and width of the first lobe of the cross-correlation contains inextricable information about the degree of colocalization and characteristic sizes and separation of colocalized clusters. At long distances, the cross-correlation flattens to a nearly horizontal baseline because the two molecule species are randomly distributed with respect to each other at long distances. The cross-correlation magnitude and distance in Fig. 6B were calculated by normalizing the cross-correlations, which are displayed in fig. S9. First, we determined that a distance of 1 µm was sufficiently far to achieve a flat baseline and then estimated the baseline by calculating the inverse-variance weighted mean of the cross-correlation from 1 to 2 µm. We defined the width of the cross-correlation as the farthest distance at which the cross-correlation reaches a value of 0.5 above the baseline. To determine the cross-correlation magnitude, we normalized each cross-correlation by its respective baseline so that all baselines are equal to 1 and calculated the maximum. All error bars are the SEM of the cross-correlations of individual cells, with errors propagated from the renormalization calculation.

Supplementary Materials
This PDF file includes:
Figs. S1 to S11

REFERENCES AND NOTES
1. B. Levine, G. Kroemer, Autophagy in the pathogenesis of disease. *Cell* **132**, 27–42 (2008).
2. N. Mizushima, B. Levine, Autophagy in mammalian development and differentiation. *Nat. Cell Biol.* **12**, 823–830 (2010).
3. T. Noda, Y. Ohsumi, Tor, a phosphatidylinositol kinase homologue, controls autophagy in yeast. *J. Biol. Chem.* **273**, 3963–3966 (1998).
4. Y. Kamada, T. Sekito, Y. Ohsumi, Autophagy in yeast: ATOR-mediated response to nutrient starvation, in *TOR* (Springer, 2004), pp. 73–84.
5. I. G. Ganley, D. H. Lam, J. Wang, X. Ding, S. Chen, X. Jiang, ULK1.ATG13.FIP200 complex mediates mTOR signaling and is essential for autophagy. *J. Biol. Chem.* **284**, 12297–12305 (2009).
6. C. H. Jung, C. B. Jun, S.-H. Ro, Y.-M. Kim, N. M. Otto, J. Cao, M. Kundu, D.-H. Kim, ULK-Atg13-FIP200 complexes mediate mTOR signaling to the autophagy machinery. *Mol. Biol. Cell* **20**, 1992–2003 (2009).
7. N. Hosokawa, T. Hara, T. Kaizuka, C. Kishi, A. Takamura, Y. Miura, S.-I. Iemura, T. Natsume, K. Takehana, N. Yamada, J.-L. Guan, N. Oshiro, N. Mizushima, Nutrient-dependent mTORC1 association with the ULK1-Atg13-FIP200 complex required for autophagy. *Mol. Biol. Cell* **20**, 1981–1991 (2009).
8. C. A. Mercer, A. Kaliappan, P. B. Dennis, A novel, human Atg13 binding protein, Atg101, interacts with ULK1 and is essential for macroautophagy. *Autophagy* **5**, 649–662 (2009).
9. D. W. Hailey, A. S. Rambold, P. Satpute-Krishnan, K. Mitra, R. Sougrat, P. K. Kim, J. Lippincott-Schwartz, Mitochondria supply membranes for autophagosome biogenesis during starvation. *Cell* **141**, 656–667 (2010).
10. M. Hamasaki, N. Furuta, A. Matsuda, A. Nezu, A. Yamamoto, N. Fujita, H. Oomori, T. Noda, T. Haraguchi, Y. Hiraoka, A. Amano, T. Yoshimori, Autophagosomes form at ER-mitochondria contact sites. *Nature* **495**, 389–393 (2013).
11. J. Biazik, P. Ylä-Anttila, H. Vihinen, E. Jokitalo, E.-L. Eskelinen, Ultrastructural relationship of the phagophore with surrounding organelles. *Autophagy* **11**, 439–451 (2015).
12. T. Hara, A. Takamura, C. Kishi, S.-I. Iemura, T. Natsume, J.-L. Guan, N. Mizushima, FIP200, a ULK-interacting protein, is required for autophagosome formation in mammalian cells. *J. Cell Biol.* **181**, 497–510 (2008).
13. Y.-Y. Chang, T. P. Neufeld, An Atg1/Atg13 complex with multiple roles in TOR-mediated autophagy regulation. *Mol. Biol. Cell* **20**, 2004–2014 (2009).
14. E. Y. W. Chan, A. Longatti, N. C. McKnight, S. A. Tooze, Kinase-inactivated ULK proteins inhibit autophagy via their conserved C-terminal domains using an Atg13-independent mechanism. *Mol. Cell. Biol.* **29**, 157–171 (2009).
15. C. A. Lamb, T. Yoshimori, S. A. Tooze, The autophagosome: Origins unknown, biogenesis complex. *Nat. Rev. Mol. Cell Biol.* **14**, 759–774 (2013).
16. E. Karanasios, S. A. Walker, H. Okkenhaug, M. Manifava, E. Hummel, H. Zimmermann, Q. Ahmed, M.-C. Domart, L. Collinson, N. T. Ktistakis, Autophagy initiation by ULK complex assembly on ER tubulovesicular regions marked by ATG9 vesicles. *Nat. Commun.* **7**, 12420 (2016).
17. E. Itakura, N. Mizushima, Characterization of autophagosome formation site by a hierarchical analysis of mammalian Atg proteins. *Autophagy* **6**, 764–776 (2010).
18. E. Karanasios, E. Stapleton, M. Manifava, T. Kaizuka, N. Mizushima, S. A. Walker, N. T. Ktistakis, Dynamic association of the ULK1 complex with omegasomes during autophagy induction. *J. Cell Sci.* **126**, 5224–5238 (2013).
19. J.-M. Park, C. H. Jung, M. Seo, N. M. Otto, D. Grunwald, K. H. Kim, B. Moriarity, Y.-M. Kim, C. Starker, R. S. Nho, D. Voytas, D.-H. Kima, The ULK1 complex mediates MTORC1 signaling to the autophagy initiation machinery via binding and phosphorylating ATG14. *Autophagy* **12**, 547–564 (2016).
20. Y. Wang, Y. Li, F. Wei, Y. Duan, Optical imaging paves the way for autophagy research. *Trends Biotechnol.* **35**, 1181–1193 (2017).
21. T. Torisu, K. Torisu, I. H. Lee, J. Liu, D. Malide, C. A. Combs, X. S. Wu, I. I. Rovira, M. M. Fergusson, R. Weigert, P. S. Connelly, M. P. Daniels, M. Komatsu, L. Cao, T. Finkel, Autophagy regulates endothelial cell processing, maturation and secretion of von Willebrand factor. *Nat. Med.* **19**, 1281–1287 (2013).
22. M. Graef, J. R. Friedman, C. Graham, M. Babu, J. Nunnari, ER exit sites are physical and functional core autophagosome biogenesis components. *Mol. Biol. Cell* **24**, 2918–2931 (2013).
23. I. Koyama-Honda, E. Itakura, T. K. Fujiwara, N. Mizushima, Temporal analysis of recruitment of mammalian ATG proteins to the autophagosome formation site. *Autophagy* **9**, 1491–1499 (2013).
24. Q. Chen, X. Shao, M. Hao, H. Fang, R. Guan, Z. Tian, M. Li, C. Wang, L. Ji, H. Chao, J.-L. Guan, J. Diao, Quantitative analysis of interactive behavior of mitochondria and lysosomes using structured illumination microscopy. *Biomaterials* **250**, 120059 (2020).
25. B. Hein, K. I. Willig, S. W. Hell, Stimulated emission depletion (STED) nanoscopy of a fluorescent protein-labeled organelle inside a living cell. *Proc. Natl. Acad. Sci. U.S.A.* **105**, 14271–14276 (2008).
26. H. Yamaguchi, S. Honda, S. Torii, K. Shimizu, K. Katoh, K. Miyake, N. Miyake, N. Fujikake, H. T. Sakurai, S. Arakawa, S. Shimizu, Wipi3 is essential for alternative autophagy and its loss causes neurodegeneration. *Nat. Commun.* **11**, 5311 (2020).
27. A. C. Nascimbeni, F. Giordano, N. Dupont, D. Grasso, M. I. Vaccaro, P. Codogno, E. Morel, ER-plasma membrane contact sites contribute to autophagosome biogenesis by regulation of local PI3P synthesis. *EMBO J.* **36**, 2018–2033 (2017).
28. S. A. Walker, E. Karanasios, N. T. Ktistakis, Correlative live cell and super resolution imaging of autophagosome formation. *Methods Enzymol.* **587**, 1–20 (2017).
29. P. Annibale, S. Vanni, M. Scarselli, U. Rothlisberger, A. Radenovic, Quantitative photo activated localization microscopy: Unraveling the effects of photoblinking. *PLOS ONE* **6**, e22678 (2011).
30. J. Gunzenhäuser, N. Olivier, T. Pengo, S. Manley, Quantitative super-resolution imaging reveals protein stoichiometry and nanoscale morphology of assembling HIV-Gag virions. *Nano Lett.* **12**, 4705–4710 (2012).
31. S.-H. Lee, J. Y. Shin, A. Lee, C. Bustamante, Counting single photoactivatable fluorescent molecules by photoactivated localization microscopy (PALM). *Proc. Natl. Acad. Sci. U.S.A.* **109**, 17436–17441 (2012).

32. E. M. Puchner, J. M. Walter, R. Kasper, B. Huang, W. A. Lim, Counting molecules in single organelles with superresolution microscopy allows tracking of the endosome maturation trajectory. *Proc. Natl. Acad. Sci. U.S.A.* **110**, 16015–16020 (2013).

33. N. Durisic, L. Laparra-Cuervo, Á. Sandoval-Álvarez, J. S. Borbely, M. Lakadamyali, Single-molecule evaluation of fluorescent protein photoactivation efficiency using an in vivo nanotemplate. *Nat. Methods* **11**, 156–162 (2014).

34. B. Van Lengerich, C. Agnew, E. M. Puchner, B. Huang, N. Jura, EGF and NRG induce phosphorylation of HER3/ERBB3 by EGFR using distinct oligomeric mechanisms. *Proc. Natl. Acad. Sci. U.S.A.* **114**, E2836–E2845 (2017).

35. C. K. Spahn, M. Glaesmann, J. B. Grimm, A. X. Ayala, L. D. Lavis, M. Heilemann, A toolbox for multiplexed super-resolution imaging of the *E. coli* nucleoid and membrane using novel PAINT labels. *Sci. Rep.* **8**, 14768 (2018).

36. E. Betzig, G. H. Patterson, R. Sougrat, O. W. Lindwasser, S. Olenych, J. S. Bonifacino, M. W. Davidson, J. Lippincott-Schwartz, H. F. Hess, Imaging intracellular fluorescent proteins at nanometer resolution. *Science* **313**, 1642–1645 (2006).

37. H. Shroff, H. White, E. Betzig, Photoactivated localization microscopy (PALM) of adhesion complexes. *Curr. Protoc. Cell Biol.* **Chapter 4**, Unit 4.21 (2008).

38. P. Sengupta, T. Jovanovic-Talisman, D. Skoko, M. Renz, S. L. Veatch, J. Lippincott-Schwartz, Probing protein heterogeneity in the plasma membrane using PALM and pair correlation analysis. *Nat. Methods* **8**, 969–975 (2011).

39. S. L. Veatch, B. B. Machta, S. A. Shelby, E. N. Chiang, D. A. Holowka, B. A. Baird, Correlation functions quantify super-resolution images and estimate apparent clustering due to over-counting. *PLOS ONE* **7**, e31457 (2012).

40. R. S. Erdmann, S. W. Baguley, J. H. Richens, R. F. Wissner, Z. Xi, E. S. Allgeyer, S. Zhong, A. D. Thompson, N. Lowe, R. Butler, J. Bewersdorf, J. E. Rothman, D. S. Johnston, A. Schepartz, D. Toomre, Labeling strategies matter for super-resolution microscopy: A comparison between HaloTags and SNAP-tags. *Cell Chem. Biol.* **26**, 584–592.e6 (2019).

41. L. Ripaud, V. Chumakova, M. Antonin, A. R. Hastie, S. Pinkert, R. Körner, K. M. Ruff, R. V. Pappu, D. Hornburg, M. Mann, F. U. Hartl, M. S. Hippa, Overexpression of Q-rich prion-like proteins suppresses polyQ cytotoxicity and alters the polyQ interactome. *Proc. Natl. Acad. Sci. U.S.A.* **111**, 18219–18224 (2014).

42. T. J. Gibson, M. Seiler, R. A. Veitia, The transience of transient overexpression. *Nat. Methods* **10**, 715–721 (2013).

43. W.-K. Cho, N. Jayanth, S. Mullen, T. H. Tan, Y. J. Jung, I. I. Cissé, Super-resolution imaging of fluorescently labeled, endogenous RNA polymerase II in living cells with CRISPR/Cas9-mediated gene editing. *Sci. Rep.* **6**, 35949 (2016).

44. A. O. Khan, V. A. Simms, J. A. Pike, S. G. Thomas, N. V. Morgan, CRISPR-Cas9 mediated labelling allows for single molecule imaging and resolution. *Sci. Rep.* **7**, 8450–8459 (2017).

45. A. S. Hansen, I. Pustova, C. Cattoglio, R. Tjian, X. Darzacq, CTCF and cohesin regulate chromatin loop stability with distinct dynamics. *eLife* **6**, e25776 (2017).

46. A. O. Khan, C. W. White, J. A. Pike, J. Yule, A. Slater, S. J. Hill, N. S. Poulter, S. G. Thomas, N. V. Morgan, Optimised insert design for improved single-molecule imaging and quantification through CRISPR-Cas9 mediated knock-in. *Sci. Rep.* **9**, 14219 (2019).

47. D. M. Shcherbakova, P. Sengupta, J. Lippincott-Schwartz, V. V. Verkhusha, Photocontrollable fluorescent proteins for superresolution imaging. *Annu. Rev. Biophys.* **43**, 303–329 (2014).

48. L. Cong, F. A. Ran, D. Cox, S. Lin, R. Barretto, N. Habib, P. D. Hsu, X. Wu, W. Jiang, L. A. Marraffini, F. Zhang, Multiplex genome engineering using CRISPR-Cas systems. *Science* **339**, 819–823 (2013).

49. J.-M. Park, D.-H. Lee, D.-H. Kim, Redefining the role of AMPK in autophagy and the energy stress response. *Nat. Commun.* **14**, 2994 (2023).

50. H. A. Benink, M. Urh, HaloTag technology for specific and covalent labeling of fusion proteins, in *Site-Specific Protein Labeling* (Springer, 2015), pp. 119–128.

51. C. G. England, H. Luo, W. Cai, HaloTag technology: A versatile platform for biomedical applications. *Bioconjug. Chem.* **26**, 975–986 (2015).

52. M. B. Stone, S. L. Veatch, Steady-state cross-correlations for live two-colour super-resolution localization data sets. *Nat. Commun.* **6**, 7347 (2015).

53. J. H. Joo, B. Wang, E. Frankel, L. Ge, L. Xu, R. Iyengar, X. Li-Harms, C. Wright, T. I. Shaw, T. Lindsten, D. R. Green, J. Peng, L. M. Hendershot, F. Kilic, J. Y. Sze, A. Audhya, M. Kundu, The noncanonical role of ULK/ATG1 in ER-to-Golgi trafficking is essential for cellular homeostasis. *Mol. Cell* **62**, 491–506 (2016).

54. N. Mizushima, A. Kuma, Y. Kobayashi, A. Yamamoto, M. Matsubae, T. Takao, T. Natsume, Y. Ohsumi, T. Yoshimori, Mouse Apg16L, a novel WD-repeat protein, targets to the autophagic isolation membrane with the Apg12-Apg5 conjugate. *J. Cell Sci.* **116**, 1679–1688 (2003).

55. B. Ronan, O. Flamand, L. Vescovi, C. Dureuil, L. Durand, F. Fassy, M.-F. Bachelot, A. Lamberton, M. Mathieu, T. Bertrand, J. P. Marquette, Y. El-Ahmad, B. Filoche-Romme, L. Schio, C. Garcia-Echeverria, H. Goulaouic, B. Pasquier, A highly potent and selective Vps34 inhibitor alters vesicle trafficking and autophagy. *Nat. Chem. Biol.* **10**, 1013–1019 (2014).

56. K. J. Petherick, O. J. L. Conway, C. Mpamhanga, S. A. Osborne, A. Kamal, B. Saxty, I. G. Ganley, Pharmacological inhibition of ULK1 kinase blocks mammalian target of rapamycin (mTOR)-dependent autophagy. *J. Biol. Chem.* **290**, 11376–11383 (2015).

57. M. Zachari, M. Longo, I. G. Ganley, Aberrant autophagosome formation occurs upon small molecule inhibition of ULK1 kinase activity. *Life Sci. Alliance* **3**, e202000815 (2020).

58. S. Adhikari, J. Moscatelli, E. M. Smith, C. Banerjee, E. M. Puchner, Single-molecule localization microscopy and tracking with red-shifted states of conventional BODIPY conjugates in living cells. *Nat. Commun.* **10**, 3400 (2019).

59. P. Annibale, S. Vanni, M. Scarselli, U. Rothlisberger, A. Radenovic, Identification of clustering artifacts in photoactivated localization microscopy. *Nat. Methods* **8**, 527–528 (2011).

60. R. Berardozzi, V. Adam, A. Martins, D. Bourgeois, Arginine 66 controls dark-state formation in green-to-red photoconvertible fluorescent proteins. *J. Am. Chem. Soc.* **138**, 558–565 (2016).

61. E. L. Axe, S. A. Walker, M. Manifava, P. Chandra, H. L. Roderick, A. Habermann, G. Griffiths, N. T. Ktistakis, Autophagosome formation from membrane compartments enriched in phosphatidylinositol 3-phosphate and dynamically connected to the endoplasmic reticulum. *J. Cell Biol.* **182**, 685–701 (2008).

62. P. D. Hsu, E. S. Lander, F. Zhang, Development and applications of CRISPR-Cas9 for genome engineering. *Cell* **157**, 1262–1278 (2014).

63. J. J.-M. Park, M. Seo, C. H. Jung, D. Grunwald, M. Stone, N. M. Otto, E. Toso, Y. Ahn, M. Kyba, T. J. Griffin, L. A. Higgins, D.-H. Kim, ULK1 phosphorylates Ser[30] of BECN1 in association with ATG14 to stimulate autophagy induction. *Autophagy* **14**, 584–597 (2018).

64. D. S. Grunwald, N. M. Otto, J. M. Park, D. Song, D.-H. Kim, GABARAPs and LC3s have opposite roles in regulating ULK1 for autophagy induction. *Autophagy* **16**, 600–614 (2020).

65. R. McGorty, D. Kamiyama, B. Huang, Active microscope stabilization in three dimensions using image correlation. *Opt. Nanoscopy* **2**, 3 (2013).

66. A. Mancebo, D. Mehra, C. Banerjee, D. H. Kim, E. M. Puchner, Efficient cross-correlation filtering of one- and two-color single molecule localization microscopy data. *Front. Bioinform.* **1**, 739769 (2021).

67. R. E. Thompson, D. R. Larson, W. W. Webb, Precise nanometer localization analysis for individual fluorescent probes. *Biophys. J.* **82**, 2775–2783 (2002).